The Astrophysical Journal, 941:174 (11pp), 2022 December 20 https://doi.org/10.3847/1538-4357/ac9da0

Uncertainty and Bias of Cosmology and Astrophysical Population Model from Statistical Dark Sirens

Hang Yu, Brian Seymour, Yijun Wang, and Yanbei Chen
TAPIR, Walter Burke Institute for Theoretical Physics, Mailcode 350-17, California Institute of Technology, Pasadena, CA 91125, USA; hyu45jhu@gmail.com
Received 2022 June 22; accepted 2022 October 18; published 2022 December 21

Abstract

Gravitational-wave (GW) radiation from a coalescing compact binary is a standard siren, as the luminosity distance of each event can be directly measured from the amplitude of the signal. One possibility to constrain cosmology using the GW siren is to perform statistical inference on a population of binary black hole (BBH) events. In essence, this statistical method can be viewed as follows. We can modify the shape of the distribution of observed BBH events by changing the cosmological parameters until it eventually matches the distribution constructed from an astrophysical population model, thereby allowing us to determine the cosmological parameters. In this work, we derive the Cramér–Rao bound for both cosmological parameters and those governing the astrophysical population model from this statistical dark siren method by examining the Fisher information contained in the event distribution. Our study provides analytical insights and enables fast yet accurate estimations of the statistical accuracy of dark siren cosmology. Furthermore, we consider the bias in cosmology due to unmodeled substructures in the merger rate and mass distribution. We find that a 1% deviation in the astrophysical model can lead to a more than 1% error in the Hubble constant. This could limit the accuracy of dark siren cosmology when there are more than 10^4 BBH events detected.

Unified Astronomy Thesaurus concepts: Cosmological parameters (339); Hubble constant (758); Gravitational wave sources (677); Stellar mass black holes (1611)

1. Introduction

The key to studying modern cosmology is to measure a relation between distance and redshift. In electromagnetic (EM) observations, the redshift to the source can be directly measured (e.g., by comparing the measured spectra to the ones obtained in terrestrial laboratories), and the challenge is to constrain the distance. To do so requires utilizing some form of standard reference. One possibility is to use "standard candles" with known intrinsic luminosity, and the best-known example is a Type Ia supernova (Riess et al. 1996, 2021). Another possibility is to use a "standard ruler" with a known size, and the imprint of sound waves in the cosmic microwave background is such an example (Spergel et al. 2003; Planck Collaboration et al. 2014, 2020). However, a tension on the value of the Hubble constant, conventionally denoted by H_0, emerges between the latest results of the two sets of measurements (Verde et al. 2019). It thus calls for a third method to either reconcile or confirm the tension.

This brings observations using gravitational waves (GWs) to people's attention, a new possibility opened up by Advanced LIGO (aLIGO; Aasi et al. 2015), Advanced Virgo (Virgo Collaboration et al. 2015), and KAGRA (Kagra Collaboration et al. 2019; Akutsu et al. 2021). The GW events are "standard sirens" in cosmology (Schutz 1986; Holz & Hughes 2005), as the amplitude of an event directly encodes the luminosity distance to the source. If the redshift information can be further constrained, we can then determine the values of cosmological parameters.

One way to obtain the redshift information is through multimessenger observation of an event. If we can simultaneously observe a GW event and its EM counterpart, corresponding to a "bright siren," we can then identify the host galaxy of the event, from which we can further extract the redshift (Holz & Hughes 2005; Chen et al. 2018). A GW event involving neutron stars (either a binary neutron star, BNS, or a neutron star–black hole event) is an ideal candidate here. Indeed, the first BNS event, GW170817, is a highly successful example (Abbott et al. 2017a, 2017b). From this event alone, we were able to constrain the Hubble constant to $H_0 = 70^{+12}_{-8}$ km s^{-1} Mpc^{-1} within the 68% credible interval. With future detectors like LIGO-Voyager (Adhikari et al. 2020) or third-generation (3G) GW detectors including the Einstein Telescope (Sathyaprakash et al. 2011) and the Cosmic Explorer (Abbott et al. 2017c; Reitze et al. 2019; Evans et al. 2021), it is potentially possible to constrain H_0 with percent-level accuracy and the normalized matter density Ω_m to an accuracy of $\mathcal{O}(10\%)$ (Chen et al. 2021). However, such bright sirens are rare, and GW170817 is the only joint observation to date. Even with 3G detectors, Califano et al. (2022) estimated that only 0.1% of detectable BNSs will have observable EM counterparts. Besides a direct EM counterpart, it is also possible to constrain cosmology from matter effects in coalescing BNSs (Messenger & Read 2012).

Alternatively, we may further utilize information in binary black hole (BBH) events, which consist of the majority of event catalogs (Abbott et al. 2016, 2019; Nitz et al. 2019; Gray et al. 2020; Nitz et al. 2020; Venumadhav et al. 2020; Abbott et al. 2021a, 2021b, 2021e; Olsen et al. 2022). An EM counterpart is typically not expected for a BBH event; therefore, a BBH corresponds to a dark siren (though a counterpart might be possible if the BBH resides in a gaseous environment; see, e.g., McKernan et al. 2019). While for a single event, it is

challenging to obtain the redshift due to the perfect degeneracy between redshift and mass (unless the source can be accurately localized to only a few potential host galaxies, a point we will get back to in Section 6), we can nonetheless infer the redshift distribution of a collection of BBH events statistically.

Initially, the statistical inference was done by comparing a BBH event catalog with galaxy catalogs (e.g., Schutz 1986; Chen et al. 2018; Fishbach et al. 2019; Finke et al. 2021). Later, people realized that features in the mass distribution of BBH events could also be used to constrain the cosmological parameters. This corresponds to "spectral sirens" (e.g., Chernoff & Finn 1993; Taylor et al. 2012; Farr et al. 2019; Abbott et al. 2021d; Mastrogiovanni et al. 2021; María Ezquiaga & Holz 2021, 2022). In both cases, one computes the likelihood of each event to happen given a set of cosmological parameters, as well as an assumed astrophysical population model. The likelihoods for all the events are then multiplied together to get the likelihood of the observed population given the assumed cosmological and astrophysical parameters. This is further converted to a posterior distribution of parameters with an assumed prior distribution (Mandel et al. 2019; Thrane & Talbot 2019).

In essence, the statistical approach corresponds to a comparison between two histograms, or distributions. One distribution is obtained from the observed BBH events with respect to either the luminosity distance or detector-frame masses (or both as a high-dimensional distribution). The other distribution is constructed from our astrophysical model with respect to either redshift or source-frame masses (or both). By varying the values of cosmological parameters, as well as those governing the astrophysical population, we can eventually match up the two distributions, thereby constraining the cosmology and population model simultaneously.

With this view, we propose an especially convenient way to assess the statistical power of dark siren cosmology. In particular, we can analytically construct the Fisher information encoded in the distributions. From that, we can both estimate the uncertainties on the parameters governing the distributions and understand the correlations among the parameters. As we will show later, even with a few simplifying assumptions, this approach predicts a similar level of uncertainty on the Hubble constant when applied to the GWTC-3 catalog (Abbott et al. 2021e), as well as many other key features obtained in LIGO Scientific Collaboration et al. (2021d). It also reproduces the results of previous studies (e.g., Fishbach et al. 2018; Farr et al. 2019) when forecasting the future constraints on both the population model and cosmology with hundreds to thousands of BBH events. Therefore, our approach serves as a simple and analytical way to study the statistical dark siren method, which can be especially useful when making quick but decently accurate predictions for the future when a large number of events are expected. It thus complements the more accurate yet also more complicated hierarchical inference approach (Mandel et al. 2019).

Furthermore, our approach can be used to study the bias on cosmological and/or astrophysical parameters due to errors in the assumed population models. We will first provide a general framework to study the bias due to any form of error; then, as a case study, we will examine in detail how unmodeled substructures in the mass and/or redshift model would affect the inference of the Hubble constant. This is motivated by the latest population model by LIGO Scientific Collaboration et al. (2021c), where signs of substructures are suggested.

The rest of the paper is organized as follows. In Section 2, we provide the mathematical framework to construct the Fisher information matrix of a distribution, which estimates the covariance matrix when jointly fitting cosmological parameters and population properties. We will also consider the bias induced on the cosmological parameters due to structures not captured by a parameterized population model with a specific functional form. We then describe the astrophysical model adopted in our study in Section 3. The application to the GWTC-3 catalog is presented in Section 4. To further validate our method, we also present the reproduction of previous studies' results using our method in the Appendix. In Section 5, we consider the bias on cosmological inference induced by unmodeled substructures in both the mass distribution and merger rate function, and we set requirements on the accuracy of the population in order for the bias to be below the statistical error. Lastly, we conclude and discuss in Section 6.

2. Basic Framework

We demonstrate in this work that in essence, the statistical dark siren approach corresponds to a comparison between a measured distribution of GW events and the one we construct based on our knowledge (or assumption) of the cosmology and the astrophysical source population.

Examples are illustrated in Figures 1 and 2. Here the y-axis is the normalized detection probability density of GW events (the parameters are consistent with those inferred from GWTC-3; Section 4). The x-axis can be the redshift z or the mass of the primary (either the detector-frame one, $m_1^{(\mathrm{d})}$, or the source-frame one, m_1). While for illustration purposes, we focus on marginalized 1D distributions, the analysis in this section can be straightforwardly extended to high-dimensional distributions as well.

Without loss of generality, we can construct a histogram of observed BBH events with respect to a general coordinate x (which can be the redshift z, the mass of the primary black hole m_1, or other quantities). The expected number of observations in the ith bin at $[x_i, x_i + \Delta x)$ can be written as $r_i(\boldsymbol{\theta}^C, \boldsymbol{\theta}^A)\Delta x$, where r is the event density. We use $\boldsymbol{\theta}^C = (H_0, \Omega_m, ...)$ to denote the cosmological parameters, and $\boldsymbol{\theta}^A$ indicates the other astrophysical parameters. The number of observations in the ith bin, n_i, follows a Poisson distribution:[1]

$$p[n_i|r_i(\boldsymbol{\theta}^C, \boldsymbol{\theta}^A)] = \frac{(r_i\Delta x)^{n_i}\exp(-r_i\Delta x)}{n_i!}. \quad (1)$$

[1] Here, for simplicity, we ignore the inference uncertainty of each individual event's parameters (e.g., redshift and mass, etc.). As we will see in later sections, the results we obtain under this simplification are decently accurate. The uncertainty on an individual event's parameters smears out fine details but keeps the broad, coarse-grained features in the population distribution. Current analysis focuses on the coarse-grained part (see, e.g., LIGO Scientific Collaboration et al. 2021d), though for high-precision cosmology, it would be critical to also capture substructures in the model (see later in Section 5). A more general treatment incorporating the uncertainty (and potentially systematic bias) on individual events is deferred to a future study.

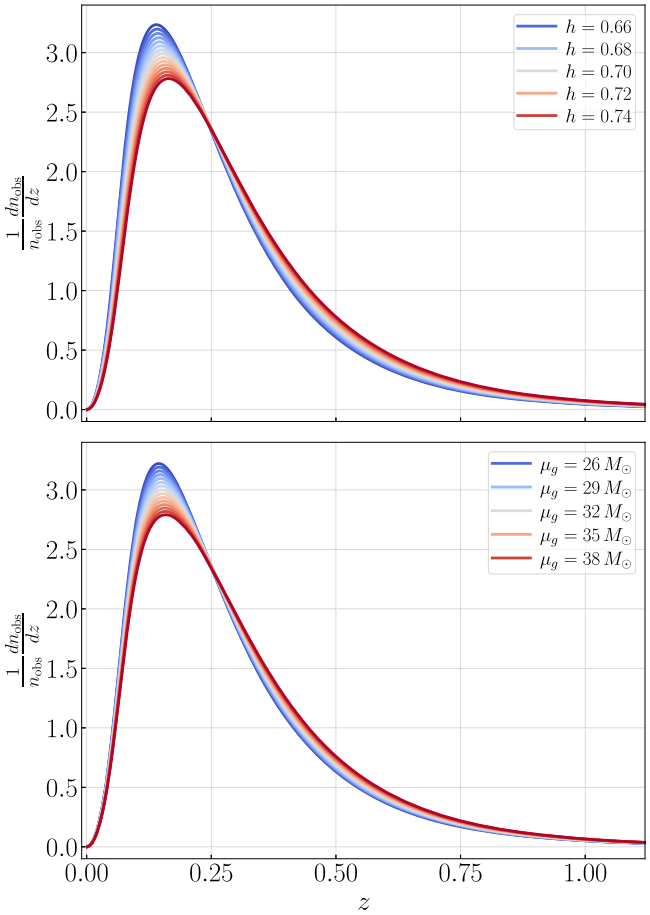

Figure 1. Top: expected number of detections as a function of the redshift z at different values of $h \equiv H_0/(100\ \mathrm{km\ s^{-1}\ Mpc^{-1}})$. From GW events, we can construct such a distribution as a function of D_L first and then convert it to a function of z based on assumed cosmological parameters. Meanwhile, our astrophysical knowledge allows us to construct an expected distribution as a function of z from, e.g., galaxy catalogs. By comparing the two histograms, we can then constrain the value of the cosmological parameters. The bottom panel shows that the distribution is also affected by astrophysical models (e.g., the location of a peak in the BBH's mass distribution μ_g; see Section 3), which could mimic the effect of changing cosmological models. This indicates the significance of jointly analyzing astrophysical and cosmological parameters.

The Fisher information of $\boldsymbol{\theta} = (\boldsymbol{\theta}^C, \boldsymbol{\theta}^A)$ at a given bin i is given by

$$\begin{aligned} I_{i,ab} &= \sum_{n_i=0}^{\infty} p[n_i|r_i(\boldsymbol{\theta})]\left[\frac{\partial \log p(n_i|r_i)}{\partial r_i}\right]^2\left[\frac{\partial r_i(\boldsymbol{\theta})}{\partial \theta_a}\right]\left[\frac{\partial r_i(\boldsymbol{\theta})}{\partial \theta_b}\right] \\ &= \left[\frac{\partial r_i(\boldsymbol{\theta})}{\partial \theta_a}\right]\left[\frac{\partial r_i(\boldsymbol{\theta})}{\partial \theta_b}\right]\sum_{n_i=0}^{\infty} p[n_i|r_i(\boldsymbol{\theta})]\left[\frac{\partial \log p(n_i|r_i)}{\partial r_i}\right]^2 \\ &= \frac{\Delta x}{r_i}\left[\frac{\partial r_i(\boldsymbol{\theta})}{\partial \theta_a}\right]\left[\frac{\partial r_i(\boldsymbol{\theta})}{\partial \theta_b}\right], \\ &= r_i\left[\frac{\partial \log r_i(\boldsymbol{\theta})}{\partial \theta_a}\right]\left[\frac{\partial \log r_i(\boldsymbol{\theta})}{\partial \theta_b}\right]\Delta x, \end{aligned} \tag{2}$$

where we have used the subscripts a, b to denote the (a, b)th element in the Fisher information matrix, and the derivatives are evaluated at the true values of $\boldsymbol{\theta}$ (or, in practice, our best estimation of $\boldsymbol{\theta}$). Summing over all of the bins and converting the discrete sum into an integral over dx, we thus arrive at the

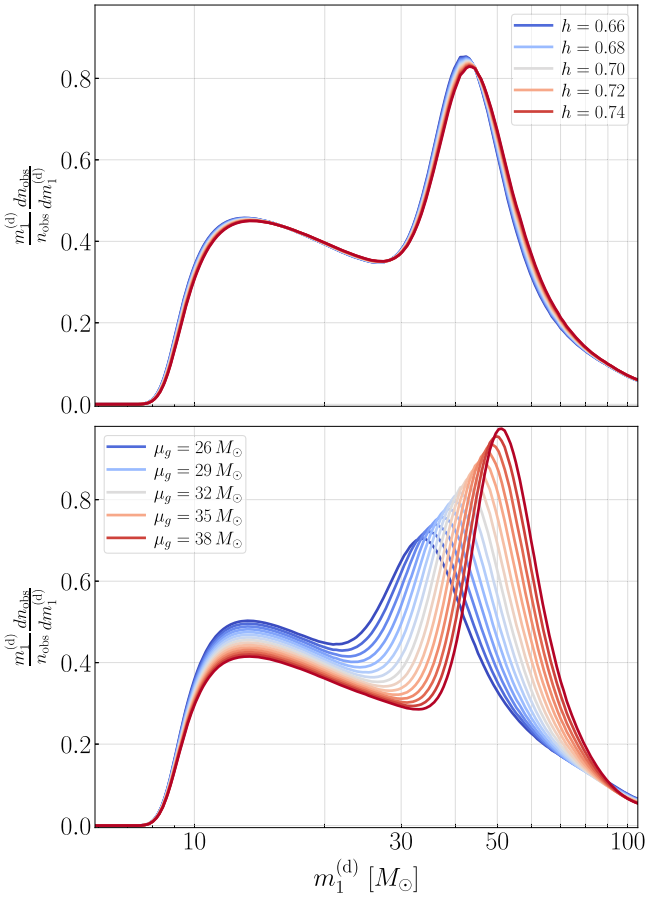

Figure 2. Similar to Figure 1, but now we plot the distribution as a function of the detector-frame mass of the primary black hole, $m_1^{\rm d}$. Combining it with Figure 1 can thus be used to break the degeneracy between astrophysical and cosmological parameters.

Fisher information matrix:

$$I_{ab}(\boldsymbol{\theta}) = \int r(x|\boldsymbol{\theta})\left[\frac{\partial \log r(x|\boldsymbol{\theta})}{\partial \theta_a}\right]\left[\frac{\partial \log r(x|\boldsymbol{\theta})}{\partial \theta_b}\right]dx. \tag{3}$$

From the distribution, the covariance matrix of $\boldsymbol{\theta}$, $\mathbf{Cov}(\boldsymbol{\theta})$, can be estimated by the Cramér–Rao bound as

$$\mathbf{Cov}(\boldsymbol{\theta}) = [\boldsymbol{I}(\boldsymbol{\theta})]^{-1}. \tag{4}$$

For future convenience, we also define $\boldsymbol{I}^C$, where the differentiation in Equation (3) is done only with respect to $\boldsymbol{\theta}^C$, or $\theta_{a,b} \in \{\boldsymbol{\theta}^C\}$. Effectively, $\boldsymbol{I}^C$ corresponds to the case where we have perfect knowledge of the astrophysical event rate, while $\boldsymbol{I}$ further considers the covariance between astrophysical population models and cosmological parameters.

Note that in the analysis above, we have assumed that the astrophysical model has the correct functional form and only has unknown parameter values. It might also be possible that the astrophysical model is formally inaccurate (e.g., due to substructures in the model and/or evolution in the population). In this case, the estimation of cosmological parameters can be systematically biased.

To calculate the bias, we suppose that the true rate (denoted by a superscript t) in the ith bin can be written as

$$r_i^t = r_i(\boldsymbol{\theta}^C, \boldsymbol{\theta}^A) + \Delta r_i. \tag{5}$$

We can expand the log-likelihood around the true $\boldsymbol{\theta}^C$ and $\Delta r_i = 0$ (the expansion around $\boldsymbol{\theta}^A$ can be straightforwardly included, but the covariance between $\boldsymbol{\theta}^A$ and $\boldsymbol{\theta}^C$ has been accounted for in the Fisher matrix in Equation (3), and therefore we ignore it here),

$$\Delta \log p = \frac{\partial^2 \log p}{\partial \theta_a^C \partial \theta_b^C}\Delta\theta_a^C \Delta\theta_b^C + \frac{\partial^2 \log p}{\partial \theta_a^C \partial r_i^t}\Delta\theta_a^C \Delta r_i + \frac{\partial^2 \log p}{\partial (r_i^t)^2}\Delta r_i^2, \quad (6)$$

where the first derivative vanishes because at true values, the probability is maximized.

The bias in the cosmological parameter induced by Δr_i is then given by setting

$$0 = \frac{\Delta \log p}{\Delta \theta_a^C}, \quad (7)$$

or

$$\frac{\partial^2 \log p}{\partial \theta_a^C \partial \theta_b^C}\Delta\theta_b^C = -\frac{\partial^2 \log p}{\partial \theta_a^C \partial r_i^t}\Delta r_i. \quad (8)$$

Computing the expectation with respect to n_i at each bin and then summing over the bins, we arrive at

$$\Delta\theta_b^C \sum_i \sum_{n_i} p(n_i|\boldsymbol{\theta}) \frac{\partial^2 \log p}{\partial \theta_a^C \partial \theta_b^C} = -\sum_i \Delta r_i \sum_{n_i} p(n_i|\boldsymbol{\theta}) \frac{\partial^2 \log p}{\partial \theta_a^C \partial r_i^t}. \quad (9)$$

If we further notice

$$\sum_{n_i} p(n_i|\boldsymbol{\theta}) \frac{\partial^2 \log p}{\partial \theta_a \theta_b} = -\sum_{n_i} p(n_i|\boldsymbol{\theta}) \frac{\partial \log p}{\partial \theta_a} \frac{\partial \log p}{\partial \theta_b}, \quad (10)$$

we arrive at

$$\Delta\boldsymbol{\theta}^C = -[\boldsymbol{I}^C]^{-1} \int \left[\frac{\partial \log r(x|\boldsymbol{\theta})}{\partial \boldsymbol{\theta}^C}\right] \Delta r(x) dx. \quad (11)$$

We can thus use Equation (11) to study how an error in the astrophysical rate model, $\Delta r(x)$, propagates to the cosmological parameters, $\boldsymbol{\theta}^C$. Note that while we focus on $\Delta\boldsymbol{\theta}^C$ in this study, our framework can also be straightforwardly extended to study the bias on astrophysical parameters.

3. Combined Astrophysical and Cosmological Model

In this section, we derive the expected event rate $r(m_1, m_2, z|\boldsymbol{\theta})$, which can then be used to construct the Fisher information (Equation (3)) and/or estimate the bias on $\boldsymbol{\theta}^C$ (Equation (11)).

Suppose the intrinsic distribution of GW events is (Fishbach et al. 2018; LIGO Scientific Collaboration et al. 2021d)

$$\frac{dn}{dm_1 dm_2 dz}(m_1, m_2, z|\boldsymbol{\theta}) = R\, p(m_1, m_2, z|\boldsymbol{\theta}), \quad (12)$$

where R is the total number of BBHs, and we normalize the probabilities such that

$$\int dm_1 dm_2 dz\, p(m_1, m_2, z|\boldsymbol{\theta}) = 1. \quad (13)$$

The expectation of the observed event density is

$$r(m_1, m_2, z|\boldsymbol{\theta}) = \frac{dn_{\rm obs}}{dm_1 dm_2 dz}(m_1, m_2, z|\boldsymbol{\theta}) = R P_{\rm det}[m_1, m_2, D_L(z|\boldsymbol{\theta}^C)] p(m_1, m_2, z|\boldsymbol{\theta}), \quad (14)$$

where D_L is the luminosity distance, and $P_{\rm det} \in [0, 1]$ is the fraction of GW events with (m_1, m_2, z) that are detectable.

The above expression is generic. To proceed, we further make simplifying assumptions following Fishbach et al. (2018) and consistent with LIGO Scientific Collaboration et al. (2021d). In particular, we assume

$$p(m_1, m_2, z|\boldsymbol{\theta}) = p(m_1, m_2|\boldsymbol{\theta}^A) p(z|\boldsymbol{\theta}^A, \boldsymbol{\theta}^C), \quad (15)$$

where $p(m_1, m_2|\boldsymbol{\theta}^A)$ describes the mass distribution, and we assume that it is independent of the redshift. The redshift distribution is then captured by $p(z|\boldsymbol{\theta}^A, \boldsymbol{\theta}^C)$. We separately normalize the two distributions as $\int p(m_1, m_2|\boldsymbol{\theta}^A) dm_1 dm_2 = 1$ and $\int p(z|\boldsymbol{\theta}^A, \boldsymbol{\theta}^C) dz = 1$.

For the rest of our study, we will focus on the case where $p(m_1, m_2|\boldsymbol{\theta}^A)$ is described by the `Power Law + Peak` model (Talbot & Thrane 2018; Abbott et al. 2021c), and we use the same notation as used in LIGO Scientific Collaboration et al. (2021d). In this case, the distribution of the mass of the primary black hole, m_1 (with $m_1 \geqslant m_2$), contains two components: a truncated power-law component defined between $(M_{\rm min}, M_{\rm max})$ with $p(m_1) \propto m_1^{-\alpha}$ and a Gaussian peak centered at μ_g with a width of σ_g. The overall height of the Gaussian peak is governed by a parameter λ_g. For a given m_1, the secondary mass then follows a truncated power law between $(M_{\rm min}, m_1)$ with a slope $p(m_2) \propto m_2^{\beta}$. Additionally, we smooth the lower end of both m_1 and m_2 with a sigmoid function defined in Equation (B7) in LIGO Scientific Collaboration et al. (2021c) and with a parameter δ_m.

For the redshift model, we further write

$$p(z|\boldsymbol{\theta}^A, \boldsymbol{\theta}^C) \propto \frac{dV_c}{dz}(z|\boldsymbol{\theta}^C) \frac{\psi(z|\boldsymbol{\theta}^A)}{1+z}, \quad (16)$$

where $V_c(z|\boldsymbol{\theta}^C)$ is the comoving volume, and the $1/(1+z)$ term converts from detector- to source-frame time. A general parameterization of the $\psi(z)$ piece can be written as (Madau & Dickinson 2014)

$$\psi(z) = [1 + (1+z_p)^{-\gamma-k}] \frac{(1+z)^{\gamma}}{1 + [(1+z)/(1+z_p)]^{\gamma+k}}, \quad (17)$$

where γ and k respectively describe the low- and high-redshift power-law slopes, and z_p corresponds to a peak in $\psi(z)$. For GWTC-3, where most events are detected at low redshifts, $\psi(z)$ simplifies to (see, e.g., Fishbach et al. 2018)

$$\psi(z) = (1+z)^{\gamma}. \quad (18)$$

We will adopt Equation (18) for our analysis and drop (z_p, k).

Under the model described above, there are nine astrophysical parameters, $\boldsymbol{\theta}^A = (M_{\rm min}, M_{\rm max}, \delta_m, \alpha, \beta, \lambda_g, \mu_g, \sigma_g, \gamma)^{\rm T}$. For the cosmological part, we assumed a flat universe described by $\boldsymbol{\theta}^C = (H_0, \Omega_m)^{\rm T}$, with H_0 the Hubble constant and Ω_m the mass density normalized by the critical density. For future convenience, we will define $h = H_0/(100\,{\rm km\,s^{-1}\,Mpc^{-1}})$.

Table 1
Values of ($\boldsymbol{\theta}^A$, $\boldsymbol{\theta}^C$) Used in Our Study to Construct the Fisher Information Matrix (Equation (3)) and Estimate the Bias Due to Δr (Equation (11))

$M_{\rm min}$	$M_{\rm max}$	δ_m	α	β	λ_g	μ_g	σ_g	γ	h	Ω_m
$6.5\,M_\odot$	$112.5\,M_\odot$	$2.5\,M_\odot$	3.78	−0.81	0.03	$32.27\,M_\odot$	$3.88\,M_\odot$	4.59	0.7	0.3

To estimate $P_{\rm det}$, we follow Fishbach et al. (2018) and approximate the observed signal-to-noise ratio (S/N) of an event as

$$\rho[m_1, m_2, D_L(z|\boldsymbol{\theta}^C)] = \rho_0\Theta, \tag{19}$$

where ρ_0 is a characteristic S/N of the source, and Θ accounts for the change in the S/N due to angular projection, with

$$\log\Theta \sim \mathcal{N}(0, \sigma^2_{\log\Theta}), \tag{20}$$

$$\sigma^2_{\log\Theta} = \frac{\sigma^2_{\log\Theta,0}}{1+\rho_0/\rho_{\rm th}}, \tag{21}$$

where $\sigma^2_{\log\Theta,0}$ and $\rho_{\rm th}$ are further parameters controlling the shape of Θ.

Suppose sources with $\rho > \rho_{\rm th}$ are detectable; we have

$$P_{\rm det} = \int_{\log\Theta_{\rm th}}^{\infty} p(\log\Theta)\,d\log\Theta = \frac{1}{2}{\rm Erfc}\left(\frac{\log\Theta_{\rm th}}{\sqrt{2}\,\sigma_{\log\Theta}}\right), \tag{22}$$

where $\Theta_{\rm th} = \rho_{\rm th}/\rho_0$, and Erfc is the complementary error function.

4. Applications to GWTC-3

In this section, we apply our method to GWTC-3 (Abbott et al. 2021e) and estimate the uncertainties on ($\boldsymbol{\theta}^A$, $\boldsymbol{\theta}^C$) when jointly fitting the astrophysical population distribution and cosmology together. Despite the simplicity of our method, it successfully captures many qualitative features and gives accurate predictions of different parameters' uncertainties as reported in LIGO Scientific Collaboration et al. (2021d). Further validation of our method can be found in the Appendix, where we also apply our method to reproduce results in Fishbach et al. (2018) and Farr et al. (2019).

Note that to evaluate the Fisher information matrix (Equation (3)), we need to take derivatives around the "true" model parameters. These values are mostly approximated by the ones inferred in LIGO Scientific Collaboration et al. (2021d), and we summarize them in Table 1. Figures 1 and 2 are also generated with the same set of parameters (except for the one listed in the legend). Note that we slightly modified the values of $M_{\rm min} = 6.5\,M_\odot$ and $\delta_m = 2.5\,M_\odot$ to make our Figure 2 more similar to Figure 1 in LIGO Scientific Collaboration et al. (2021d).[2] The overall scale R is set so that the total number of BBH detections is $n_{\rm obs} = \int r(m_1, m_2, z|\boldsymbol{\theta})dm_1dm_2dz = 40$, consistent with the number of BBH events used in LIGO Scientific Collaboration et al. (2021d).

To approximate $P_{\rm det}$, we compute the characteristic ρ_0 using a single detector with LIGO Hanford's sensitivity in the third observing run (Buikema et al. 2020) for each $[m_1, m_2, D_L(z|\boldsymbol{\theta}^C)]$. The waveform is generated with the IMRPhenomD approximation (Khan et al. 2016; the waveform is computed using `PYCBC`; Nitz et al. 2022), and the source is placed at an effective distance of $2.3D_L$ (Allen et al. 2012). We further use $\rho_{\rm th} = 8$ and $\sigma^2_{\log\Theta,0} = 0.25$ when computing Equation (22).

4.1. Using Redshift Distribution while Holding Population Model Fixed

First, we consider the case where we constrain the cosmological parameters using the redshift distribution of BBH events while treating the underlying astrophysical population as known and fixed. An astrophysical expectation can be constructed using the coarse-grained distribution of galaxies. Indeed, when each BBH event is localized with limited accuracy and thousands of galaxies or more lie within the uncertainty volume, a galaxy catalog mainly serves as an estimation of the overall smoothed shape of $\psi(z)$, which we model as a simple power law as in Equation (18). In this case, cosmological parameters are constrained by requesting consistency between the distribution of observed BBH events and our astrophysical expectation, as demonstrated in the top panel of Figure 1. (We will return to this in Section 6 to discuss how improved localization accuracy, together with a complete galaxy catalog, could help.)

In Figure 3, we present the constraints on (h, Ω_m) from the marginalized redshift distribution $r(z|\boldsymbol{\theta}) = \int r(m_1, m_2, z|\boldsymbol{\theta})dm_1dm_2$ (cf. Figure 1). The result is obtained by inverting a 3×3 Fisher matrix involving (h, Ω_m, R) and treating $\boldsymbol{\theta}^A$ as known (Equation (3) with x replaced by z). Our approach predicts an uncertainty in h of 0.11, nicely agreeing with the results shown in Figure 9 in LIGO Scientific Collaboration et al. (2021d). On the other hand, Ω_m is not well constrained (in fact, its error is greater than its true value, and thus it exceeds the capability of the Fisher matrix) because of both the relatively small sample size ($n_{\rm obs} = 40$) and the fact that most events are detected at low redshift with $z < 0.5$.

However, as pointed out in, e.g., LIGO Scientific Collaboration et al. (2021d and Mastrogiovanni et al. (2021)) and illustrated in Figure 1, the constraints on the cosmological parameters rely critically on the assumptions of the astrophysical model. We elaborate on this point further in Figure 4 in the cyan error ellipses. We obtained these ellipses by inverting a 3×3 Fisher matrix involving (h, μ_g, R) in the top panel and one involving (h, γ, R) in the bottom panel. We notice strong anticorrelations between h and μ_g and between h and γ, consistent with the results shown in LIGO Scientific Collaboration et al. (2021d). This demonstrates that with the redshift distribution of BBH events alone, measuring cosmological parameters can be challenging unless we have highly precise knowledge of the intrinsic population model.

4.2. Jointly Fitting Astrophysical Population Model and Cosmology

Fortunately, besides the redshift distribution itself, we also have information on other properties of BBH events, such as

[2] There are likely two peaks in the mass distribution as suggested in LIGO Scientific Collaboration et al. (2021c), and the lower one (around $m_1 = 10\,M_\odot$) is not captured by the `Power Law + Peak` model adopted by LIGO Scientific Collaboration et al. (2021d).

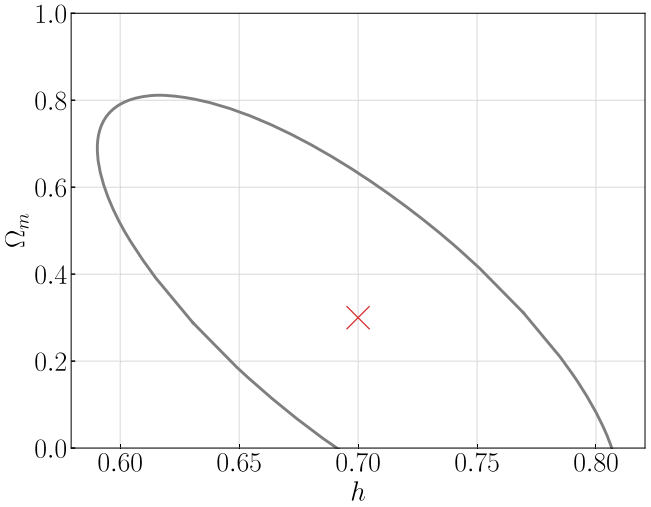

Figure 3. Uncertainties on cosmological parameters (h, Ω_m) from the redshift histogram (cf. Figure 1), assuming we know the astrophysical model exactly. Throughout this work, we will use red crosses to denote the true values of the parameters (i.e., the values at which we evaluate the Fisher information matrix). The error ellipses indicate the 68% credible intervals. We predict an uncertainty on h of ± 0.11, which agrees well with the gray dotted curve in Figure 9 in LIGO Scientific Collaboration et al. (2021d) obtained under the same assumptions.

the mass distribution. As demonstrated in Figure 2, the partial degeneracy between h and μ_g shown in redshift distribution (Figure 1) can be largely broken once we include the distribution of the detector-frame mass distribution of the primary, $r[m_1^{(d)}|\boldsymbol{\theta}] = \int [r(m_1, m_2, z)/(1+z)] dm_2 dz$.

Similar to how we obtain the cyan ellipses in Figure 4, we also construct Fisher matrices for (h, μ_g, R) in the top panel (or (h, γ, R) in the bottom panel) from the $m_1^{(d)}$ distribution. The results are shown by the orange ellipses. Since distributions of both z and $m_1^{(d)}$ are available in a GW catalog, we can combine them together, leading to the gray ellipses in Figure 4. This allows us to individually constrain h and μ_g to good accuracy (assuming other parameters in $\boldsymbol{\theta}$ are known), and the covariance between h and γ can also be significantly reduced.

Combining the Fisher information from the redshift and mass distributions together is largely similar to the hierarchical inference performed in LIGO Scientific Collaboration et al. (2021d). To illustrate this point, we now invert the full Fisher matrix (note that in Figure 4, we considered only submatrices), and the results are shown in Figure 5. More specifically, we construct two Fisher matrices using Equation (3) with x respectively substituted by z and $m_1^{(d)}$. The two matrices are summed together and then inverted to give us the gray error ellipses.

Overall, our result shows nice agreement with the one reported in LIGO Scientific Collaboration et al. (2021d). In particular, the 68% credible interval for h is $h = 0.70 \pm 0.29$, and it exhibits a strong anticorrelation with γ and $M_{\rm max}$, whose uncertainties are also consistent with Figure 5 in LIGO Scientific Collaboration et al. (2021d). Because we used a simple approximation of $P_{\rm det}$ (Equations (19)–(22)) and ignored the statistical error on each individual event, we do not expect an exact reproduction of the results in LIGO Scientific Collaboration et al. (2021d). Due to our simplifying treatments, μ_g is better constrained than in LIGO Scientific Collaboration et al. (2021d), and its correlation with h, as well as with other parameters, is lifted (see also Figure 4 and note that the gray

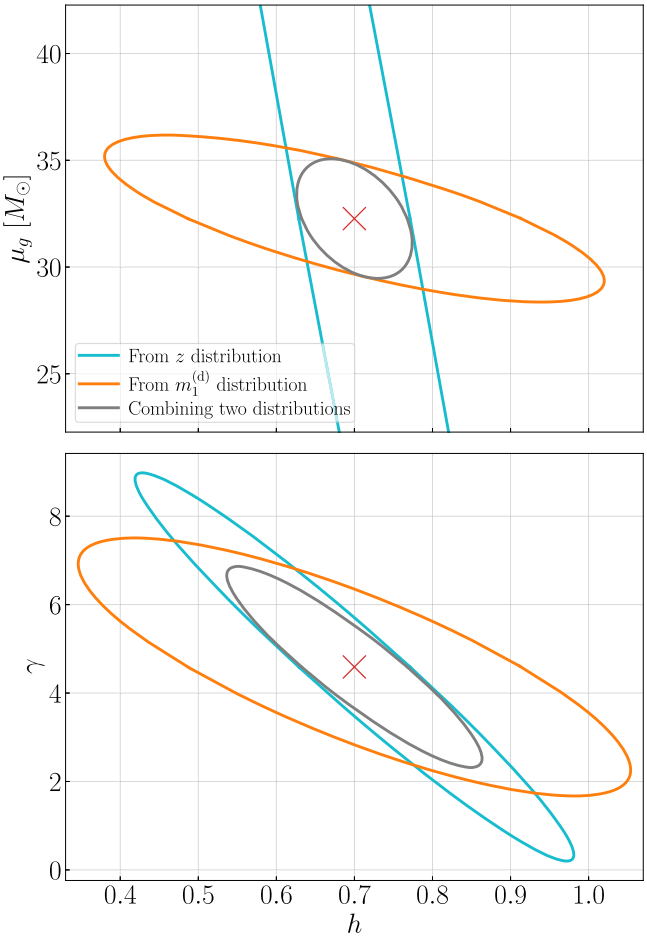

Figure 4. Correlation between astrophysical and cosmological parameters by inverting a 3×3 Fisher matrix including (h, μ_g, R) (top panel) or (h, γ, R) (bottom panel). The cyan ellipses correspond to constraints from the redshift distribution alone (cf. Figure 1). As μ_g and/or γ decreases, h will increase to a greater value. It captures the key features shown in Figure 10 in LIGO Scientific Collaboration et al. (2021d). If one further incorporates the information from the mass distribution (orange ellipses; cf. Figure 2), the combined uncertainties can be reduced to the gray ellipses.

error ellipse in the top panel is much smaller than the one in the bottom panel).

In fact, we can directly construct a Fisher matrix from a three-dimensional (3D) distribution $r(m_1, m_2, z|\boldsymbol{\theta})$. This leads to the olive ellipses in Figure 5. This contains more information and thus leads to tighter constraints on parameters compared to combining two marginalized distributions (gray ellipses). For GWTC-3 with only slightly more than 40 BBH events, however, we do not have a high S/N in the 3D histogram $r(m_1, m_2, z|\boldsymbol{\theta})$.[3] Therefore, summing the marginalized distribution in z and $m_1^{(d)}$ (gray ellipses) provides a better agreement of GWTC-3 results (LIGO Scientific Collaboration et al. 2021d) than the 3D distribution (olive ellipses). Nonetheless, as the sample size increases, we would expect that the 3D distribution

[3] Consider a discrete example. We would need at least eight different bins to constrain ($M_{\rm min}$, $M_{\rm max}$, δ_m, α, λ_g, μ_g, σ_g) in the histogram of m_1 or $m_1^{(d)}$. For the secondary mass m_2, we would additionally need two more bins to determine the power-law slope β. The redshift distribution requires at least three bins to constrain (γ, h). Thus, a full 3D histogram would require more than 48 bins. This is greater than the sample size used by LIGO Scientific Collaboration et al. (2021d). Nonetheless, there will be enough events to populate the 3D histogram when aLIGO reaches its designed sensitivity and detects $\mathcal{O}(1000)$ events yr^{-1} (as assumed in, e.g., Farr et al. 2019).

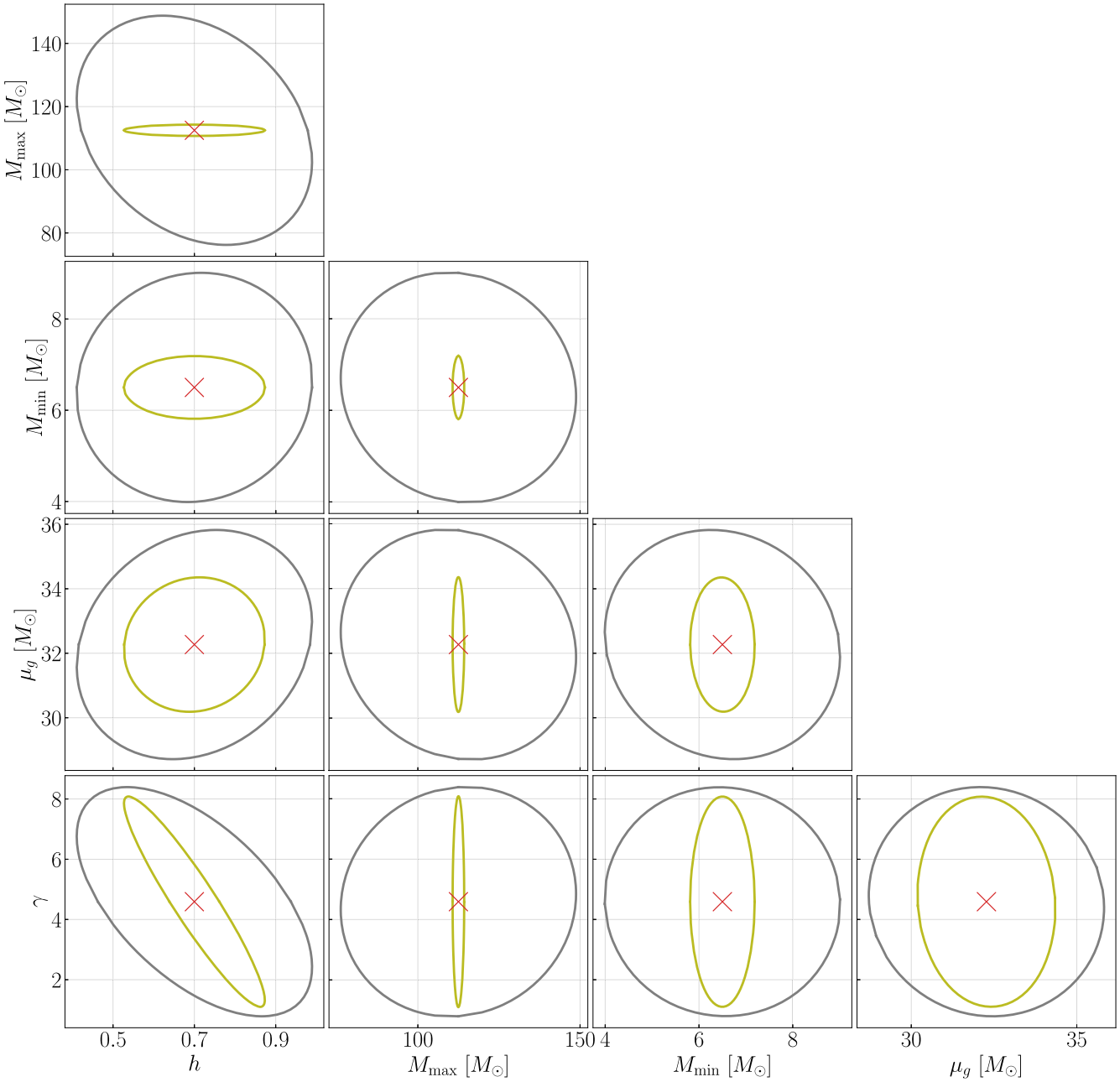

Figure 5. Error ellipses for a sample of 40 BBH events similar to the GWTC-3 catalog. The gray ellipses are obtained by summing the Fisher information from the marginalized redshift and primary mass distribution together, and the olive ones are from the 3D $r(m_1, m_2, z)$ distribution.

becomes a more accurate prediction (which we validate in the Appendix by reproducing the results in Fishbach et al. 2018 and Farr et al. 2019). Therefore, in addition to the $1/\sqrt{n}_{\rm obs}$ reduction in the uncertainties (as obviously seen in Equations (3) and (14)), we would expect the results reported in LIGO Scientific Collaboration et al. (2021d) to improve further from the gray ellipses to the olive ones as the S/N of each bin in the 3D distribution increases (with the expectation of the bin becoming greater than its Poissonian error; see footnote [3]). This can be especially valuable for constraining $M_{\max}$, as changing it can significantly alter $P_{\rm det}$ at large redshift, a point we will illustrate further when discussing the bias on cosmological parameters.

5. Bias Induced by Substructures in the Population Model

Having discussed in the previous section the parameter estimation uncertainties when jointly fitting the cosmological and astrophysical models, we now consider the bias in the cosmological parameters (especially H_0) induced by inaccuracies in our astrophysical model, which is naturally expected if our parameterized model is insufficient to capture all the details in the true population model. Indeed, we note that the specific functional form assumed in our study (the `Power Law + Peak` model) is not significantly preferred over, e.g., a broken power-law model (LIGO Scientific Collaboration et al. 2021d). More possibilities with different parameterizations are also considered in, e.g., LIGO Scientific Collaboration et al. (2021c) and Roulet et al. (2021). Furthermore, the mass distribution could contain more complicated features (Tiwari & Fairhurst 2021)

and/or be redshift-dependent (Mukherjee 2022; Karathanasis et al. 2022; Mapelli et al. 2022; van Son et al. 2022), introducing more features beyond what is captured by the model described in Section 3. Similarly, an error in the redshift model $\psi(z)$ could also bias the inferred cosmology (You et al. 2021).

Suppose the true event density can be written as

$$r^t(m_1, m_2, z) = RP_{\rm det} \times [(1 - \Delta r_0)p(m_1, m_2, z|\boldsymbol{\theta}) + \Delta r_0 p_{\rm err}(m_1, m_2, z)], \quad (23)$$

and our parameterized model captures the $r = RP_{\rm det}p(m_1, m_2, z|\boldsymbol{\theta})$ part. This leads to an error of

$$\Delta r(m_1, m_2, z) = \Delta r_0[RP_{\rm det}p_{\rm err}(m_1, m_2, z) - r(m_1, m_2, z)], \quad (24)$$

where $p_{\rm err}$ specifies the shape of the deviation and is normalized to $\int p_{\rm err}(m_1, m_2, z)dm_1dm_2dz = 1$, and Δr_0 is an overall factor governing the magnitude of the deviation. We note further that the $-r$ term only affects the overall number of GW events when plugged into Equation (11) and therefore can be absorbed by a rescaling of R; when $\Delta r_0 > 0$, it decreases the value of R. For the rest of the section, we will focus on the effect induced by $p_{\rm err}$.

In particular, we focus on bias induced by unmodeled local substructures. For this, we write

$$p_{\rm err}(m_1, m_2, z) = p_{\rm err}(m_1, m_2)p_{\rm err}(z), \quad (25)$$

with

$$p_{\rm err}(m_1, m_2) \propto \frac{1}{m_1 - M_{\rm min}} \exp\left[\frac{-(m_1 - \mu_{m,\rm err})^2}{2\sigma^2_{m,\rm err}}\right], \quad (26)$$

$$p_{\rm err}(z) \propto \frac{1}{1+z}\frac{dV_c}{dz} \exp\left[\frac{-(z - \mu_{z,\rm err})^2}{2\sigma^2_{z,\rm err}}\right], \quad (27)$$

where the location of the substructure is governed by $\mu_{m,\rm err}$ and $\mu_{z,\rm err}$ and the width by $\sigma_{m,\rm err}$ and $\sigma_{z,\rm err}$. In our study, we vary $(\mu_{m,\rm err}, \mu_{z,\rm err})$ and fix $\sigma_{m,\rm err} = 1\,M_\odot$ and $\sigma_{z,\rm err} = 0.025$. As a brief aside, we note that the local error considered here can serve as a building block for considering more extended errors, as a generic Δr can be viewed as the superposition of many such local substructures.

To set the overall factor Δr_0, we request

$$\frac{\Delta r_0 \int P_{\rm det}p_{\rm err}dm_1dm_2dz}{\int P_{\rm det}dm_1dm_2dz} = 0.01. \quad (28)$$

In other words, we assume that the unmodeled substructure contains 1% of the BBH events. Note that we choose $\Delta r_0 > 0$ for the simplicity of our discussion; Δr_0 can be either positive (a local peak) or negative (a local trough).

In this section, we follow Fishbach et al. (2018) and approximate $P_{\rm det}$ according to the aLIGO design sensitivity. In particular, we approximate the characteristic S/N as

$$\rho_0 = 8\left[\frac{\mathcal{M}_c(1+z)}{10\,M_\odot}\right]^{5/6}\left(\frac{1\ {\rm Gpc}}{D_L}\right), \quad (29)$$

where $\mathcal{M}_c = m_1^{3/5}m_2^{3/5}/(m_1 + m_2)^{1/5}$ is the chirp mass of the BBH. Following Fishbach et al. (2018), we further set $\rho_{\rm th} = 8$ and $\sigma^2_{\log\Theta,0} = 0.3$ in Equation (21).

We are now ready to evaluate the bias due to Δr (Equation (24)) on cosmological parameters according to Equation (11). Here we focus on the bias on h, and we consider $\boldsymbol{\theta}^C = (h, R)^{\rm T}$ in Equation (11). The result is shown in Figure 6.

First, we note that the bias is independent of $n_{\rm obs}$. This is because in Equation (11), we have $[\boldsymbol{I}^C]^{-1} \propto n_{\rm obs}^{-1}$, whereas $\Delta r \propto n_{\rm obs}$. This is in contrast to the statistical uncertainty discussed in Section 4, which reduces as $n_{\rm obs}^{-1/2}$. Therefore, while we expect a significant reduction in the statistical uncertainty as current detectors become increasingly more sensitive, and 3G GW detectors like Cosmic Explorer (Reitze et al. 2019) and the Einstein Telescope (Sathyaprakash et al. 2011) come online in the 2030s, the systematic bias will persist unless we incorporate more sophisticated models. In particular, we would expect to detect 15,000 BBH events every month with a 3G detector (Vitale et al. 2019). This means that we would reduce the statistical error on h to the subpercent level within a month of observation according to Figure 5. This is below the bias shown in Figure 6; therefore, the dark siren cosmology would be limited by uncertainties in our astrophysical population model.

We further note that for large $\mu_{m,\rm err}$ and small $\mu_{z,\rm err}$ (bottom right part of Figure 6), the bias is nearly a constant. The bias then gradually decreases and becomes negative as $\mu_{m,\rm err}$ decreases and $\mu_{z,\rm err}$ increases, or as we go to the top left part of Figure 6. The transition is characterized by the line of $\rho_0 = 8$ (brown dotted line in Figure 6), where we have used $m_1 = m_2 = \mu_{m,\rm err}$ to evaluate $\mathcal{M}_c$ and $\mu_{z,\rm err}$ to evaluate D_L in Equation (29).

These features can be understood as follows. Because we assume that $p_{\rm err}$ is caused by local substructures and model it as a multivariate Gaussian in m_1 and z (and uniform in m_2), from Equation (11), the bias is approximately given by[4]

$$\Delta h \propto \frac{\partial \log r(\mu_{m,\rm err}, \mu_{m,\rm err}, \mu_{z,\rm err}|\boldsymbol{\theta})}{\partial h}, \sim \frac{\partial \log P_{\rm det}}{\partial h} + \frac{\partial \log(dV_c/dz)}{\partial h}, \quad (30)$$

where in the second line, we have selected out the terms that have nonvanishing derivatives with respect to h, and those values are approximately evaluated at $(m_1, m_2, z) = (\mu_{m,\rm err}, \mu_{m,\rm err}, \mu_{z,\rm err})$.

In the bottom right part of Figure 6, $P_{\rm det} \simeq 1$. Thus, the only contribution to Δh comes from $\partial\log(dV_c/dz)/\partial h = 3/h$, which is a constant. This is why the bias is nearly constant in this region. Physically, the excess events contained in Δr make us infer a greater comoving volume than the true value at a given redshift, which then leads to a positive bias in h.

As we move toward the top left part of Figure 6, $P_{\rm det}$ changes from 1 to zero. Numerically, the slope is the steepest when $\Theta_{\rm th} = \rho_{\rm th}/\rho_0$ is around 1. Because changing h changes the

[4] Here we treat $p(z)$ as an unnormalized function and use R to absorb the normalization to simplify the discussion. Note that h and R are not completely degenerate because of $P_{\rm det}$, which can be seen from Figure 1. In the real calculation, we include both h and R in $\boldsymbol{\theta}^C$ and hence $\boldsymbol{I}^C$ when evaluating Equation (11) to account for the correlation between them arising from this freedom in the definition of $p(z)$ and R.

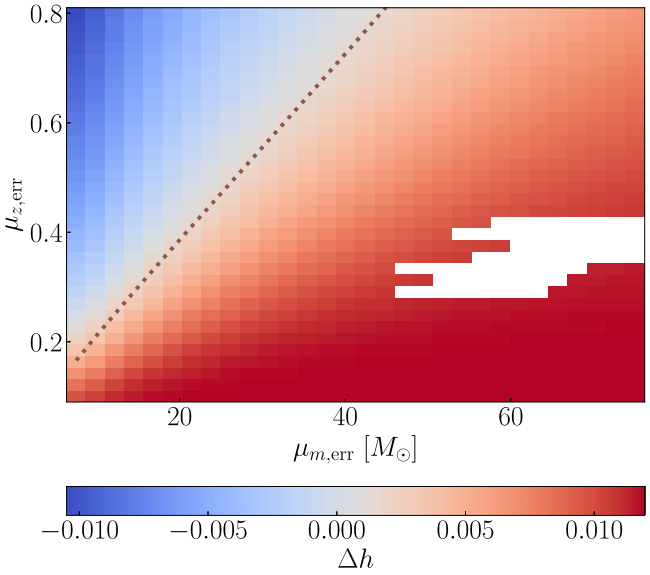

Figure 6. Bias on h due to an error in the astrophysical rate Δr given by Equations (25)–(27). An error in m_1 but constant in redshift can then be obtained by summing over all the pixels along a specific $\mu_{m,\mathrm{err}}$ (i.e., a vertical line) with appropriate normalization. Likewise, other generic Δr can be obtained by summing over the corresponding pixels. Also shown with the dotted brown line is an approximation of the detection threshold with $[\mathcal{M}_c(1+z)]^{5/6}/z \simeq$ constant.

value of ρ_0 at a given redshift $\mu_{z,\mathrm{err}}$, the $\partial \log P_{\mathrm{det}}/\partial h$ term in Equation (30) now starts to contribute. This drives the bias Δh to a more negative value. Depending on the location, a local substructure containing 1% of BBH events could bias the estimation of h by about 1% in either the positive or negative direction. As we mentioned above, the statistical error on h will drop below 1% with about 10^4 events. This is likely beyond aLIGO's expected detection number, yet it can be easily achieved with 3G detectors. Our study thus sets the requirements of the accuracy of our astrophysical population model in the 3G era.

6. Conclusion and Discussion

In this study, we derived the Cramér–Rao bound of both astrophysical and cosmological parameters from the distributions (both marginalized and high-dimensional) of BBH events. Our approach complements the hierarchical inference currently employed by, e.g., LIGO Scientific Collaboration et al. (2021d). Its analytical simplicity makes it especially useful in predicting the performance of future detectors and providing insights into the statistics.

The basic framework to both perform joint astrophysical and cosmological parameter estimations and compute bias in the parameters due to errors in the assumed model was presented in Section 2. The specific population model in our analysis was introduced in Section 3, which we then applied to place constraints on a BBH sample similar to GWTC-3 in Section 4. In particular, we found that the GWTC-3 results can be well reproduced if we combine the Fisher information of both the BBHs' redshift distribution and the mass distribution together. In the future, tighter constraints (in addition to the $\sqrt{n_{\mathrm{obs}}}$ reduction in the errors) would be expected, as more events would allow us to construct an accurate 3D distribution of BBH events in the (m_1, m_2, z) space. Then, in Section 5, we further considered the bias induced by unmodeled substructures in the population model. The bias due to other forms of Δr can be readily obtained by summing over the relevant pixels in Figure 6 with proper reweighting. For instance, a substructure in m_1 but constant in z can be obtained by summing along a vertical line in Figure 6. If the error Δr contains 1% of the observed population, it could easily bias the estimation in the Hubble constant by more than 1%. Therefore, to achieve a high-precision cosmology from a statistical dark siren, it would require a high level of accuracy in the astrophysical model with fine details captured.

Note further that our Equation (11) applies not only to cosmological parameters but also to astrophysical ones, as we can simply replace $\boldsymbol{\theta}^C$ with $\boldsymbol{\theta}^A$ or any other subset of $\boldsymbol{\theta}$. This could be of astrophysical significance. For example, the location of the mass gap due to pair-instability supernovae could be biased by substructures produced by dynamical formation channels or the redshift dependence in the mass function (Mukherjee 2022; Karathanasis et al. 2022; María Ezquiaga & Holz 2022). Our Equation (11) thus provides a simple and analytical way to quantify the bias.

As a first step, our current model does not include the statistical error on each individual event's component mass and luminosity distance. This may be a subdominant effect for events that are well above the detection threshold, which are typically the ones selected for population studies (see, e.g., LIGO Scientific Collaboration et al. 2021d, 2021c; Roulet et al. 2021). Intuitively, the uncertainty on each event's parameters slightly blurs the measured distribution and smears out sharp features. Yet, since both $p(m_1, m_2)$ and $p(z)$ are smooth functions in our study (and in LIGO Scientific Collaboration et al. 2021d), such a blurring should not be significant (but see the discussion below on galaxy catalogs). However, information on the population is also contained in sources that are marginally detectable (or undetectable; see the discussion in Roulet et al. 2020). These events could happen at locations where P_{det} has large derivatives with respect to $\boldsymbol{\theta}$ and thus may potentially contribute to the Fisher information. To utilize them properly, incorporating their parameter estimation errors would be critical, and we plan to investigate this in a follow-up study.

We also assumed that the galaxy catalog provides only the smoothed shape of the redshift model $p(z)$. This is the case because the GW event localization accuracy is currently limited. In the other limit where a BBH could be localized to a single host galaxy (which can be achieved with a decihertz spaceborne detector; Kuns et al. 2020), a dark siren would effectively behave like a bright BNS event with an EM counterpart identified because the host galaxy in this case can be identified from the sky localization (Chen and Holz 2016; Borhanian et al. 2020; Seymour et al. 2022). This could lead to a strong constraint in cosmology (Chen et al. 2018) without needing assumptions in the underlying population model. In the intermediate case, an accurate localization plus a complete galaxy catalog could mean sharp spikes in $p(z)$ and therefore $r(z)$. Whereas h can be nearly degenerate with an overall power-law slope γ in $\psi(z)$ (which is also the limiting factor on how well we can measure h; Figure 5), it could hardly be confused with sharp spikes. Therefore, the constraints on h could thus be improved. Besides using the location of each individual event, the spatial clustering of BBH events is yet another possibility to enhance our constraint on cosmology and reduce its systematic errors (Scelfo et al. 2020; Mukherjee et al. 2021; Cigarrán Díaz & Mukherjee 2022; Mukherjee et al. 2022). A more

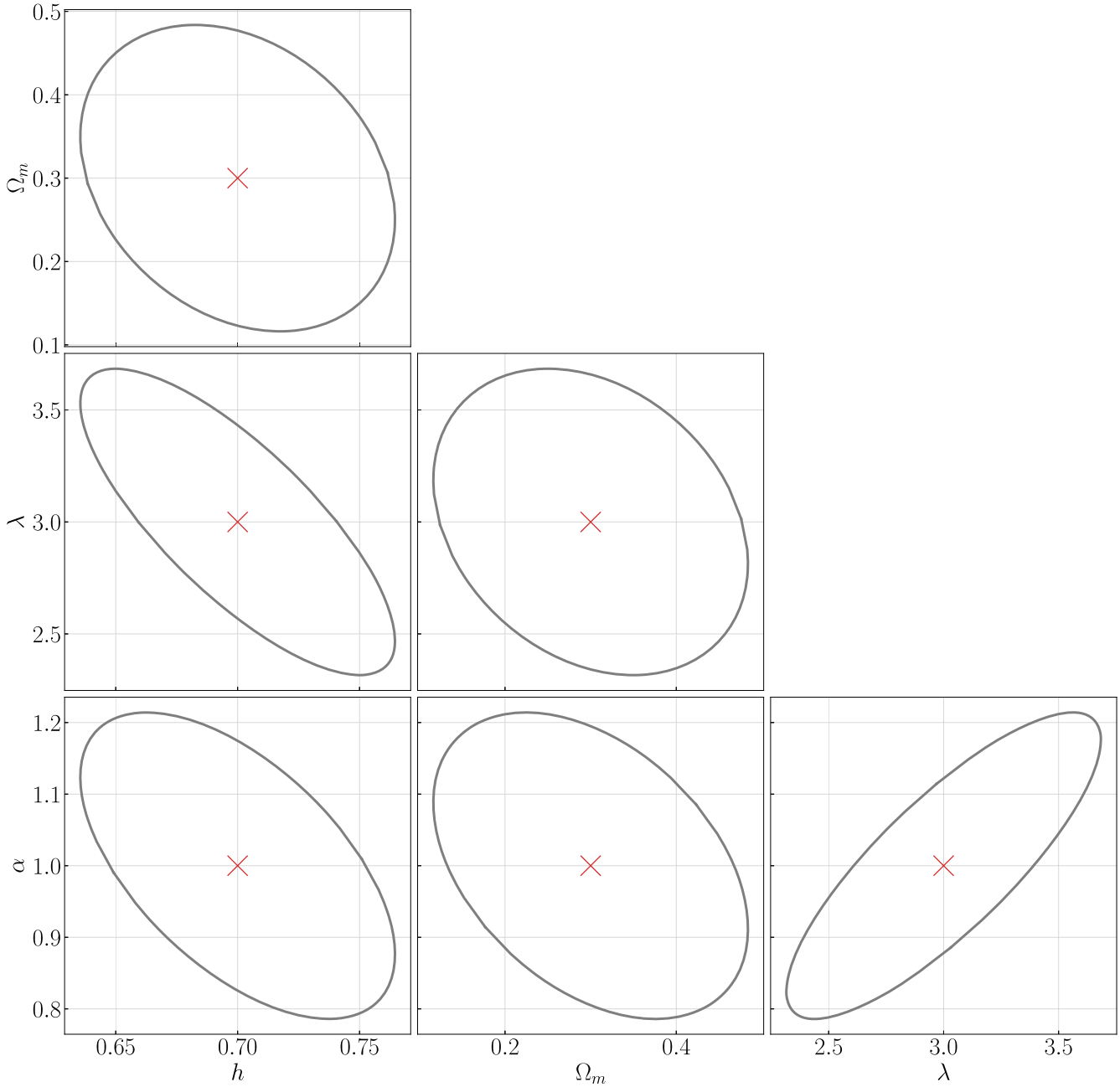

Figure 7. Error ellipses from the 3D $r(m_1, m_2, z)$ distribution assuming 500 BBH events using the model in Fishbach et al. (2018). Our results show good agreement with those obtained in Fishbach et al. (2018) and Farr et al. (2019). It thus validates our approach when $n_{\rm obs}$ is large.

quantitative study incorporating these effects coherently is to be carried out in future investigations.

We thank Katerina Chatzioannou, Hsin-Yu Chen, and the LVC colleagues for helpful discussions and comments during the preparation of the manuscript. This material is based upon work supported by NSF's LIGO Laboratory, which is a major facility fully funded by the National Science Foundation. H.Y. acknowledges the support of the Sherman Fairchild Foundation. Y.C., B.S., and Y.W. acknowledge support from the Brinson Foundation, the Simons Foundation (award No. 568762), and NSF grants PHY-2011961, PHY-2011968, and PHY-1836809.

Software: `Python3` (Van Rossum & Drake 2009), `NumPy` (Harris et al. 2020), `SciPy` (Virtanen et al. 2020), `Matplotlib` (Hunter 2007), `PYCBC` (Nitz et al. 2022).

Appendix
Validation of the Methodology

In this Appendix, we further validate our approach by reproducing some results from Fishbach et al. (2018) and Farr et al. (2019).

Following Fishbach et al. (2018), here we consider a truncated power-law mass model given by

$$p(m_1, m_2|\alpha, M_{\rm max}) \propto \frac{m_1^{-\alpha}}{m_1 - 5\,M_\odot}\mathcal{H}(M_{\rm max} - m_1), \qquad \text{(A1)}$$

where $\mathcal{H}$ is the Heaviside function, and the existence of an upper mass gap $M_{\max}$ is motivated by the pair-instability supernovae (Fowler & Hoyle 1964). Since our focus here is to reproduce the results of Fishbach et al. (2018), we use this mass model despite the fact that it is currently unfavored by the latest data (LIGO Scientific Collaboration et al. 2021d; Abbott et al. 2021c; Roulet et al. 2021). The $\psi(z)$ part in the redshift model (Equation (16)) is given by Equation (18). We particularly adopt $(\alpha, M_{\max}, \lambda) = (1, 40\,M_{\odot}, 3)$ in our calculation. The $P_{\rm det}$ is computed following Section 5 (see Equations (22) and (29)).

In Figure 7, we present the 68% credible interval for the key parameters based on the Fisher information matrix, Equation (3), with $n_{\rm obs} = 500$. In particular, we highlight the bottom right corner of Figure 7, where we show the error ellipse for (λ, α). We notice a positive correlation between the two quantities, and their uncertainties are, respectively, $\Delta\lambda = 0.68$ and $\Delta\alpha = 0.21$. Both results show nice agreement with the top left panel of Figure 5 in Fishbach et al. (2018). Moreover, because in the mass model (Equation (A1)), there is a clear feature set by $M_{\max}$, it allows the determination of h as proposed in, e.g., Farr et al. (2019) and demonstrated in the leftmost column of Figure 7. Consistent with Farr et al. (2019), we note that the uncertainty on h from 500 events is $\Delta h = 0.065$. The consistency between our Figure 7 and previous studies thus validates our approach in constraining both the astrophysical and cosmological parameters.

ORCID iDs

Hang Yu https://orcid.org/0000-0002-6011-6190
Brian Seymour https://orcid.org/0000-0002-7865-1052
Yijun Wang https://orcid.org/0000-0002-5581-2001

References

Aasi, J., Abbott, B. P., Abbott, R., et al. 2015, CQGra, 32, 074001
Abbott, B. P., Abbott, R., Abbott, T. D., et al. 2017a, ApJL, 848, L12
Abbott, B. P., Abbott, R., Abbott, T. D., et al. 2017b, Natur, 551, 85
Abbott, B. P., Abbott, R., Abbott, T. D., et al. 2017c, CQGra, 34, 044001
Akutsu, T., Ando, M., Arai, K., et al. 2021, PTEP, 2021, 05A101
Adhikari, R. X., Arai, K., Brooks, A. F., et al. 2020, CQGra, 37, 165003
Allen, B., Anderson, W. G., Brady, P. R., Brown, D. A., & Creighton, J. D. E. 2012, PhRvD, 85, 122006
Borhanian, S., Dhani, A., Gupta, A., Arun, K. G., & Sathyaprakash, B. S. 2020, arXiv:2007.02883
Buikema, A., Cahillane, C., Mansell, G. L., et al. 2020, PhRvD, 102, 062003
Califano, M., de Martino, I., Vernieri, D., & Capozziello, S. 2022, MNRAS, 518, 3372
Chen, H. -Y., Cowperthwaite, P. S., Metzger, B. D., & Berger, E. 2021, ApJL, 908, L4
Chen, H. -Y., Fishbach, M., & Holz, D. E. 2018, Natur, 562, 545
Chen, H.-Y., & Holz, D. E. 2016, arXiv:1612.01471
Chernoff, D. F., & Finn, L. S. 1993, ApJL, 411, L5
Cigarrán Díaz, C., & Mukherjee, S. 2022, MNRAS, 511, 2782
Evans, M., Adhikari, R. X., Afle, C., et al. 2021, arXiv:2109.09882
Farr, W. M., Fishbach, M., Ye, J., & Holz, D. E. 2019, ApJL, 883, L42
Finke, A., Foffa, S., Iacovelli, F., Maggiore, M., & Mancarella, M. 2021, JCAP, 2021, 026
Fishbach, M., Holz, D. E., & Farr, W. M. 2018, ApJL, 863, L41
Fishbach, M., Gray, R., Hernandez, I. M., et al. 2019, ApJL, 871, L13
Fowler, W. A., & Hoyle, F. 1964, ApJS, 9, 201
Gray, R., Hernandez, I. M., Qi, H., et al. 2020, PhRv, 101, 122001
Harris, C. R., Millman, K. J., van der Walt, S. J., et al. 2020, Natur, 585, 357
Holz, D. E., & Hughes, S. A. 2005, ApJ, 629, 15
Hunter, J. D. 2007, CSE, 9, 90
Kagra Collaboration, Akutsu, T., Ando, M., et al. 2019, NatAs, 3, 35
Karathanasis, C., Mukherjee, S., & Mastrogiovanni, S. 2022, arXiv:2204.13495
Khan, S., Husa, S., Hannam, M., et al. 2016, PhRvD, 93, 044007
Kuns, K. A., Yu, H., Chen, Y., & Adhikari, R. X. 2020, PhRvD, 102, 043001
Abbott, B. P., Abbott, R., Abbott, T. D., et al. 2016, PhRvX, 6, 041015
Abbott, B. P., Abbott, R., Abbott, T. D., et al. 2019, PhRvX, 9, 031040
Abbott, R., Abbott, T. D., Abraham, S., et al. 2021a, PhRvX, 11, 021053
Abbott, R., Abbott, T. D., Acerneses, F., et al. 2021b, arXiv:2108.01045
Abbott, R., Abbott, T. D., Abraham, S., et al. 2021c, ApJL, 913, L7
Abbott, R., Abe, H., Acernese, F., et al. 2021d, arXiv:2111.03604
Abbott, R., Abbott, T. D., Acernese, F., et al. 2021e, arXiv:2111.03606
Madau, P., & Dickinson, M. 2014, ARA&A, 52, 415
Mandel, I., Farr, W. M., & Gair, J. R. 2019, MNRAS, 486, 1086
Mapelli, M., Bouffanais, Y., Santoliquido, F., Arca?Sedda, M., & Artale, M. C. 2022, MNRAS, 511, 5797
María Ezquiaga, J., & Holz, D. E. 2021, ApJL, 909, L23
María Ezquiaga, J., & Holz, D. E. 2022, PhRvL, 129, 061102
Mastrogiovanni, S., Leyde, K., Karathanasis, C., et al. 2021, PhRvD, 104, 062009
McKernan, B., Ford, K. E. S., Bartos, I., et al. 2019, ApJL, 884, L50
Messenger, C., & Read, J. 2012, PhRvL, 108, 091101
Mukherjee, S. 2022, MNRAS, 515, 5495
Mukherjee, S., Krolewski, A., Wandelt, B. D., & Silk, J. 2022, arXiv:2203.03643
Mukherjee, S., Wandelt, B. D., Nissanke, S. M., & Silvestri, A. 2021, PhRvD, 103, 043520
Nitz, A., Harry, I., Brown, D., et al. 2022, gwastro/pycbc: v2.0.4 release of PyCBC, v2.0.4 Zenedo doi:10.5281/zenodo.6646669
Nitz, A. H., Capano, C., Nielsen, A. B., et al. 2019, ApJ, 872, 195
Nitz, A. H., Dent, T., Davies, G. S., et al. 2020, ApJ, 891, 123
Olsen, S., Venumadhav, T., Mushkin, J., et al. 2022, PhRvD, 106, 043009
Ade, P. A. R., Aghanim, N., Armitage-Caplan, C., et al. 2014, A&A, 571, A16
Aghanim, N., Akrami, Y., Ashdown, M., et al. 2020, A&A, 641, A6
Reitze, D., Adhikari, R. X., Ballmer, S., et al. 2019, BAAS, 51, 35
Riess, A. G., Casertano, S., Yuan, W., et al. 2021, ApJL, 908, L6
Riess, A. G., Press, W. H., & Kirshner, R. P. 1996, ApJ, 473, 88
Roulet, J., Chia, H. S., Olsen, S., et al. 2021, PhRvD, 104, 083010
Roulet, J., Venumadhav, T., Zackay, B., Dai, L., & Zaldarriaga, M. 2020, PhRvD, 102, 123022
Sathyaprakash, B., Abernathy, M., Acernese, F., et al. 2011, arXiv:1108.1423
Scelfo, G., Boco, L., Lapi, A., & Viel, M. 2020, JCAP, 2020, 045
Schutz, B. F. 1986, Natur, 323, 310
Seymour, B., Yu, H., & Chen, Y. 2022, arXiv:2208.01668
Spergel, D. N., Verde, L., Peiris, H. V., et al. 2003, ApJS, 148, 175
Talbot, C., & Thrane, E. 2018, ApJ, 856, 173
Taylor, S. R., Gair, J. R., & Mandel, I. 2012, PhRvD, 85, 023535
Thrane, E., & Talbot, C. 2019, PASA, 36, e010
Tiwari, V., & Fairhurst, S. 2021, ApJL, 913, L19
Van Rossum, G., & Drake, F. L. 2009, Python 3 Reference Manual (Scotts Valley, CA: CreateSpace) https://dl.acm.org/doi/book/10.5555/1593511
van Son, L. A. C., de Mink, S. E., Callister, T., et al. 2022, ApJ, 931, 17
Venumadhav, T., Zackay, B., Roulet, J., Dai, L., & Zaldarriaga, M. 2020, PhRvD, 101, 083030
Verde, L., Treu, T., & Riess, A. G. 2019, NatAs, 3, 891
Virgo Collaboration, et al. 2015, CQGra, 32, 024001
Virtanen, P., Gommers, R., Oliphant, T. E., et al. 2020, NatMe, 17, 261
Vitale, S., Farr, W. M., Ng, K. K. Y., & Rodriguez, C. L. 2019, ApJL, 886, L1
You, Z.-Q., Zhu, X.-J., Ashton, G., Thrane, E., & Zhu, Z.-H. 2021, ApJ, 908, 215